JACS Au
AN OPEN ACCESS JOURNAL OF THE AMERICAN CHEMICAL SOCIETY

pubs.acs.org/jacsau

Article

Design of Crystalline Reduction−Oxidation Cluster-Based Catalysts for Artificial Photosynthesis

Xiao-Xin Li,[⊥] Lei Zhang,[⊥] Jiang Liu,* Lin Yuan, Tong Wang, Jun-Yi Wang, Long-Zhang Dong, Kai Huang, and Ya-Qian Lan*

Cite This: *JACS Au* 2021, 1, 1288−1295

Read Online

ABSTRACT: Metal cluster-based compounds have difficulty finishing the photocatalytic carbon dioxide reduction reaction (CO_2RR) and water oxidation reaction (WOR) simultaneously because of the big challenge in realizing the coexistence of independently and synergistically reductive and oxidative active sites in one compound. Herein, we elaborately designed and synthesized one kind of crystalline reduction−oxidation (**RO**) cluster-based catalysts connecting reductive $\{M_3L_8(H_2O)_2\}$ (M = Zn, Co, and Ni for **RO-1**, **2**, **3** respectively) cluster and oxidative $\{PMo_9V_7O_{44}\}$ cluster through a single oxygen atom bridge to achieve artificial photosynthesis successfully. These clusters can all photocatalyze CO_2-to-CO and H_2O-to-O_2 reactions simultaneously, of which the CO yield of **RO-1** is 13.8 μmol/g·h, and the selectivity is nearly 100%. Density functional theory calculations reveal that the concomitantly catalytically reductive and oxidative active sites (for CO_2RR and WOR, respectively) and the effective electron transfer between the sites in these **RO** photocatalysts are the key factors to complete the overall photosynthesis.

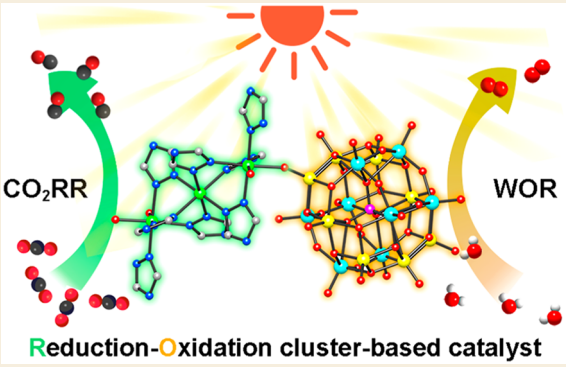

KEYWORDS: *polyoxometalates, crystalline materials, **RO** cluster-based photocatalysts, CO_2 reduction reaction, artificial photosynthesis*

INTRODUCTION

Effective coupling of photocatalytic carbon dioxide reduction reaction (CO_2RR) and water oxidation reaction (WOR) to achieve artificial photosynthesis (with water as a hole scavenger) is the most important and green means to recycle atmospheric CO_2.[1−5] Both CO_2RR and WOR are multielectron and multiproton transfer processes in which the photocatalysts are responsible for supplying multiple electrons, and water can serve as an abundant source of protons.[6,7] Currently, photocatalysts mainly include enzymes,[8,9] nanosemiconductors,[10−15] organic semiconductors,[16−18] and crystalline coordination compounds,[19−21] of which metal cluster-based coordination compounds[22−24] often show distinct advantages owing to their rich redox capabilities, tunable structures, and abilities to being multielectron donors or acceptors. In particular, their well-defined crystalline structural information is helpful to survey the photocatalytic reaction mechanism and structure−function relationship accurately.[25−27] So far, however, a single metal cluster-based coordination compound has difficulty accomplishing CO_2RR and WOR concurrently because of the challenges in realizing the coexistence of reductive and oxidative sites as well as the effective charge transfer between the catalytic sites. That is also the reason why most metal cluster-based catalysts could only achieve the half-reaction of artificial photosynthesis with the assistance of an additional sacrificial agent (triethylamine, triethanolamine for CO_2RR or $AgNO_3$ for WOR, etc.).[28−30] If one designed and constructed a crystalline reduction−oxidation (**RO**) cluster-based coordination compound by connecting reductive clusters and oxidative clusters through effective linkers (bridging atoms or conductive ligands), it would strongly promote the charge transfer between the active sites of CO_2RR and WOR and would be expected to accomplish artificial photosynthesis.

In view of the above design ideas, we think that such new **RO** cluster-based catalysts for artificial photosynthesis should fulfill at least two conditions as follows: (i) excellent light-absorption and explicit catalytic active centers with enough reductive and oxidative capabilities to complete the CO_2RR and WOR half-reactions, respectively; (ii) suitable linkers between reductive and oxidative clusters for efficient electron transfer, etc. Furthermore, the synthesis conditions of **RO** cluster-based compounds should be adaptive for the growth of reductive and oxidative components and their further assembling. Polyox-

Received: April 26, 2021
Published: July 8, 2021

https://doi.org/10.1021/jacsau.1c00186
JACS Au 2021, 1, 1288−1295

ometalates (POMs), known as "electronic sponges", have the advantages of multielectron donors and structural stability, which have widespread applications due their active metal ions with high valence states.[31−34] Therefore, POMs can be considered as the "oxidation" part in **RO** clusters. Meanwhile, because POM-based coordination polymers were usually synthesized by hydrothermal methods at high temperature,[35,36] the growth conditions of the "reduction" part would better be similar. According to our survey, the classical linear trinuclear cluster $\{\mathbf{M_3L_xS_{12-x}}\}$ (M = the first transition low-valent metal ions, L = azole ligands, S = solvent molecules, x = 6−8) are readily available and usually have good reducibility and stability.[37−40] Importantly, the two terminal metal ions coordinated with two/three solvent molecules in $\{\mathbf{M_3}\}$ can serve as efficient reductive active sites after linking with POMs.

Based on the above considerations, the linear trinuclear $\{\mathbf{M_3L_8(H_2O)_2}\}$, M = Zn, Co, Ni, L = 1,4-di(4*H*-1,2,4-triazol-4-yl)benzene (p-tr$_2$Ph), simplified as $\mathbf{M_3}$, as a reduction cluster and the phosphovanadomolybdate ($\{PMo_9V_7O_{44}\}$) as an oxidation cluster were taken into account to construct three crystalline **RO** cluster-based photocatalysts, $Zn_3(H_2O)_2(p\text{-tr}_2Ph)_5PMo_9V_7O_{44}$ (**RO-1**), $Co_3(H_2O)_2(p\text{-tr}_2Ph)_5PMo_9V_7O_{44}$ (**RO-2**), and $Ni_3(H_2O)_2(p\text{-tr}_2Ph)_5PMo_9V_7O_{44}$ (**RO-3**). Compared with the traditional α-Keggin POM, the phosphovanadomolybdate $\{PMo_9V_7O_{44}\}$ has more advantages in oxidative catalytic reactions for its more positive redox potential.[41,42] Ultraviolet−visible-near-infrared (UV−vis-NIR) spectra revealed that **RO-1**, **2**, and **3** all had a broad range of light absorption in 250−2500 nm. As expected, on account of strong redox ability and suitable band structures for reducing CO_2 to CO coupling with oxidizing H_2O to O_2, artificial photosynthetic overall reaction was successfully realized when **RO-1**, **2**, and **3** were used as photocatalysts. Among them, **RO-1** exhibits the highest CO yield of 138 μmol/g along with the O_2 evolution in a gas−solid system among reported crystalline photocatalysts. Density functional theory (DFT) calculation uncovered that the photogenerated electrons were efficiently transferred from $\{PMo_9V_7O_{44}\}$ to $\{\mathbf{M_3}\}$ under light irradiation, and CO_2-to-CO and H_2O-to-O_2 reactions were finished by $\{\mathbf{M_3}\}$ and $\{PMo_9V_7O_{44}\}$, respectively, which were in line with our initial expectation and subsequent characterizations. More importantly, this work proposes a novel design strategy to establish crystalline **RO** cluster-based catalysts to achieve the artificial photosynthetic overall reaction.

RESULTS AND DISCUSSION

Characterization of RO-1, 2, and 3 Photocatalysts

X-ray crystallography diffraction indicated that **RO-1**, **2**, and **3** are isostructural and crystallize in the triclinic system with a $\bar{P}1$ space group (Table S1). **RO-1**, **2**, and **3** consist of $\{\mathbf{M_3}\}$ ($\mathbf{Zn_3}$, $\mathbf{Co_3}$, and $\mathbf{Ni_3}$) as the reduction component and $\{PMo_9V_7O_{44}\}$ as the oxidation component, respectively (Figure 1a and b). The asymmetric unit of **RO-1**, **2**, and **3** contains 1/2 of a $\{PMo_9V_7O_{44}\}$ node, 2 metal ions, 2.5 p-tr$_2$Ph ligands, 1 coordinated H_2O molecule, and several free H_2O molecules (Figure S1). There are two kinds of metal coordinated environments in the $\{\mathbf{M_3}\}$ cluster. The M1 ion is six-coordinated with four N atoms from ligands, one O1 atom from $\{PMo_9V_7O_{44}\}$ and one O1w atom from the coordinated H_2O molecule. The M2 ion employs a common octahedron geometry surrounded with six N atoms from six p-tr$_2$Ph ligands. There are three kinds of coordination environments of p-tr$_2$Ph in the

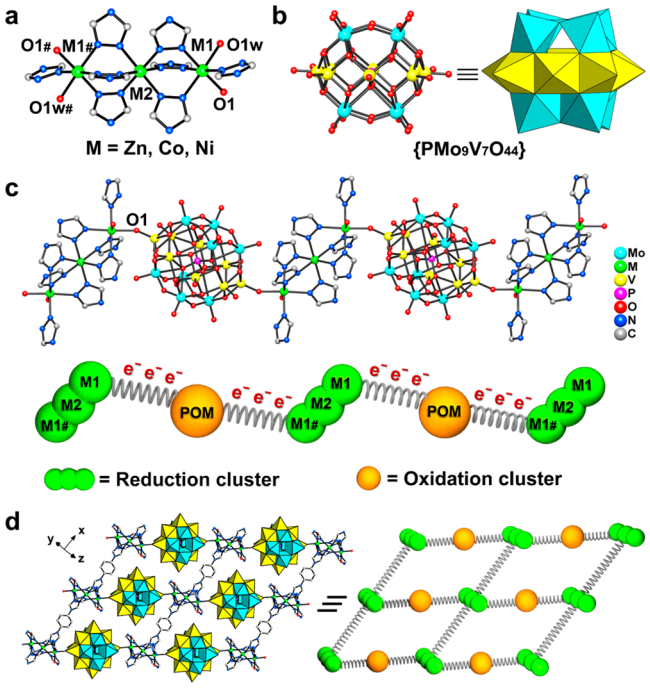

Figure 1. Summary of the structure of **RO-1**, **2**, and **3**. (a) Coordination environments of the $\{\mathbf{M_3}\}$ node. (b) Structure of the $\{PMo_9V_7O_{44}\}$ node. (c) 1D chain constructed from reduction clusters ($\{\mathbf{M_3}\}$) and oxidation cluster ($\{PMo_9V_7O_{44}\}$). (d) Spatial arrangement and corresponding to simplify the diagram. All hydrogen atoms are omitted for clarity. Mo, cyan; M, green; V, yellow; P, pink; O, red; N, blue; C, gray.

structure (Figure S2). $\{PMo_9V_7O_{44}\}$ can be considered as a heteroatom α-Keggin POM with four additional capping metal ions in the equatorial position (Figures 1b and S3). Sixteen metal ions are located at three layers from top to bottom in a "4 + 8 + 4" configuration, of which the first and third layers are all Mo ions. The second layer composes seven V ions and one Mo ion (the positions of two metal atoms are occupied by Mo atom and V atom in a disorderly fashion, and the chemical occupancy is close to 0.5). The $\{PMo_9V_7O_{44}\}$ node links with the $\{\mathbf{M_3}\}$ cluster by V−O−M bonds forming a zigzag chain (Figure 1c). Each $\{\mathbf{M_3}\}$ cluster links with four other $\{\mathbf{M_3}\}$ clusters through ligands to constitute a 2D layer (Figure S4). In the cavity of layers, $\{PMo_9V_7O_{44}\}$, as pillars, were encapsulated and connected with two $\{\mathbf{M_3}\}$ clusters from adjacent layers to assemble into a 3D layer−pillar framework (Figures 1d and S5). Owing to the restriction of single-crystal X-ray diffraction (SCXRD) methods for distinguishing elements of V, Co, Ni, and Zn, X-ray photoelectron spectroscopy (XPS) and inductively coupled plasma (ICP) are measured to verify the existence and abundance ratios of Mo, V, Zn, Co, and Ni elements. XPS spectra confirmed the existence of Mo, V, Zn (**RO-1**), Co (**RO-2**), and Ni (**RO-3**) elements in the structures, respectively (Figure S6). ICP results further determined that the stoichiometric ratios of Mo/V/M (M = Zn, Co, Ni) in **RO-1**, **2**, and **3** are all close to 9:7:3 (Table S2). Besides, high-resolution peaks of the Mo 3d spectra are located in the same positions in **RO-1**, **2**, and **3** of Mo $3d_{5/2}$ (ca. 232.5 eV) and Mo $3d_{3/2}$ (ca. 235.5 eV), validating the presence of the Mo^{V} and Mo^{VI} in these three compounds (Figures S7 and S8). Likewise, the high-resolution V 2p peaks of **RO-1**, **2**, and **3** reveal in the

https://doi.org/10.1021/jacsau.1c00186
JACS Au 2021, 1, 1288−1295

same region of V 2p (ca. 517.0 eV), demonstrating the single presence of V^{IV} (Figure S9).

Powder X-ray diffraction (PXRD) patterns of the experimental **RO-1**, **2**, and **3** were well-matched with the simulated curves from SCXRD, which proved the high purity of the samples (Figure S10). Furthermore, when **RO-1**, **2**, and **3** were immersed into 1 M HCl and 0.01 M NaOH aqueous solution for 24 h at room temperature, no peaks changed in PXRD patterns, attesting that these RO cluster-based compounds have excellent chemical stability (Figure S11, S12). Thermogravimetric analysis (TGA) exhibited that **RO-1**, **2**, and **3** have similar weight decreasing platforms and good thermostability below 300 °C (Figure S13).

The light absorption of photocatalysts was examined by UV−vis−NIR diffuse reflectance spectroscopy. It is noted that $H_3PMo_{12}O_{40}{\cdot}xH_2O$ has light response with wavelengths in the ranges 250−450 and 1400−2500 nm. In contrast, **RO-1**, **2**, and **3** have an obviously spectral range across the entire absorption region (250−2500 nm), which can be attributed to the introduction of V ions in polyoxometalate and electronic transfer after assembling with the reduction cluster (Figures 2a and S14). Such wide ranges of light absorption cause **RO-1**, **2**, and **3** all to appear black (Figures 2a inset, S15, and S16). The band gap energy of **RO-1**, **2**, and **3** were further determined to be 1.80 (**RO-1**), 1.82 (**RO-2**), and 1.88 eV (**RO-3**) by Taus plots (Figures 2b, S17, and S18), demonstrating that they have semiconductor-like characteristics. To evaluate the oxidation ability of **RO-1**, **2**, and **3**, the highest occupied molecular orbital (HOMO) energy levels, which equal the ionization potential, were calculated to be 1.16 (**RO-1**), 1.22 (**RO-2**) and 1.23 V (**RO-3**) (vs normal hydrogen electrode (NHE), pH = 7) by ultraviolet photoelectron spectroscopy (UPS) (Figures 2c, S19, and S20).[43] All the HOMO energy levels are more positive than the oxidation potential of O_2/H_2O (0.82 V vs NHE, pH = 7),[44,45] which indicated that **RO-1**, **2**, and **3** could achieve H_2O-to-O_2 catalysis thermodynamically. On this basis, the lowest unoccupied molecular orbital (LUMO) energy levels were evaluated to be −0.64, −0.60, and −0.65 V for **RO-1**, **2**, and **3**, respectively, suggesting that they are able to convert CO_2 to most chemical fuels like CO (−0.51 V vs NHE), CH_4 (−0.24 V vs NHE), and so on.[46] In additional, to verify the LUMO energy levels accurately, Mott−Schottky plots were performed at frequencies of 1000, 1500, and 2000 Hz (Figures S21−S23). The values were calculated to be −0.64 (**RO-1**), −0.61 (**RO-2**), and −0.66 V (**RO-3**) vs NHE, which are consistent with those obtained from E_g and UPS results. According to the results of bandgap, UPS, and Mott−Schottky plots, the band structure diagrams of **RO-1**, **2**, and **3** were obtained (Figure 2d), which indicated that **RO-1**, **2**, and **3** can theoretically catalyze the artificial photosynthetic overall reaction.

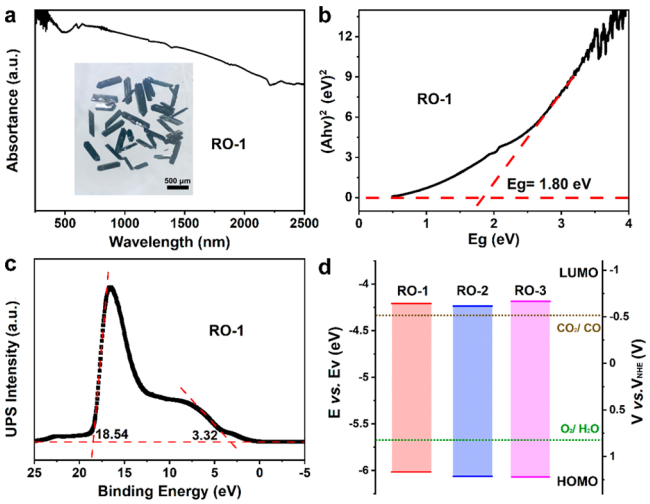

Figure 2. Optical characterizations of photocatalysts. (a) UV−vis−NIR absorption spectrum of **RO-1**. (inset) Photograph of **RO-1** under an optical microscope. (b) Band gap energy (E_g) analysis of **RO-1**. The intersection of the baseline and the slant dashed line is the band gap. (c) UPS spectrum of **RO-1**. (d) Energy bandgap diagrams of **RO-1**, **2**, and **3** with respect to the CO_2RR and WOR potentials (pH = 7). The electron volts (eV, left *y* axis) are converted to electrochemical energy potentials in volts (V, right *y* axis) according to which 0 V vs RHE (reversible hydrogen electrode) equals −4.44 eV vs evac (vacuum level). Then, the RHE potentials are further converted to NHE (pH = 7) according to E (vs NHE, pH = 7) = E (vs RHE) − 0.0591 × 7.

Catalytic Performance of Artificial Photosynthesis

On account of the above-mentioned suitable band structure, we considered that these crystalline **RO** cluster-based compounds can be used as catalysts to conduct artificial photosynthesis. All the CO_2RRs were investigated in the gas−solid system under light irradiation (λ = 300−1100 nm) without additional cocatalyst, photosensitizer, or sacrificial agent (experimental details are described in the Photocatalytic Experiments section). **RO-1**, **2**, and **3** showed high performance and selectivity of CO_2-to-CO conversion only with the participation of water vapor. By testing CO yields at 2 h intervals, roughly linear curves were obtained by gas chromatography (GC) analysis (Figure 3a, S24,

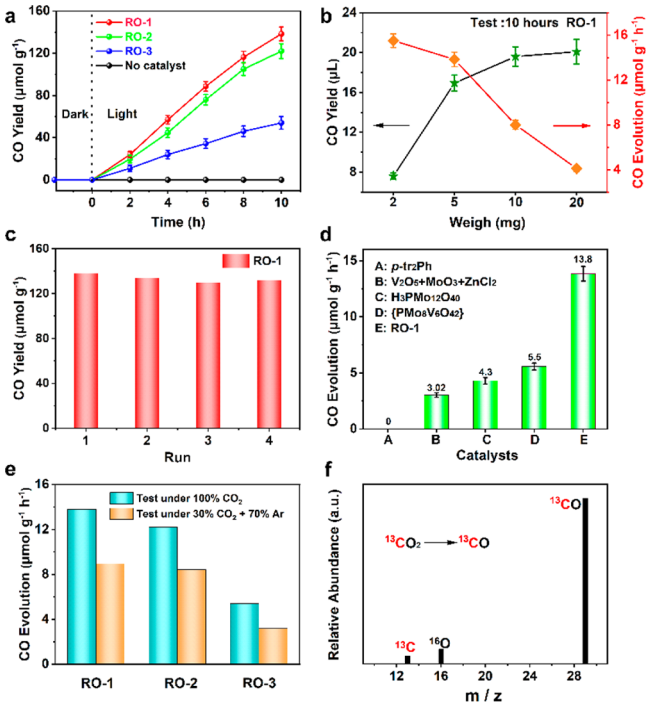

Figure 3. Photochemical performance of CO_2RR by using different photocatalysts. (a) Time-dependent CO yield of **RO-1**, **2**, and **3**. (b) Relationship between yield and rate of CO generation in different quality of **RO-1**. (c) Yield of CO for **RO-1** as a CO_2RR photocatalyst in four continuous runs. (d) Yield of CO in a series of comparison tests. (e) Comparison of the CO generation of **RO-1**, **2**, and **3** under atmospheres of 100% CO_2 and 30% CO_2 (+ 70% Ar). (f) Mass spectrum of generated ^{13}CO under $^{13}CO_2$ catalyzed by **RO-1**.

https://doi.org/10.1021/jacsau.1c00186
JACS Au 2021, 1, 1288−1295

and S25). When **RO-1** was used as a photocatalyst, the amount of CO rose to 138 μmol/g after 10 h, which is higher than 122 μmol/g for **RO-2** and more than three times higher for **RO-3** (42 μmol/g). A trace amount of CH_4 (<1 μmol/g) was detected in the gas phase. Additionally, H_2 as a competitive product was not produced during the reaction (Figure S26). In order to detect the yield of O_2 and compare it with that of CO, we performed photocatalytic tests in an online evaluation system. The results showed that the molar ratio of CO to O_2 were all close to 2/1 along with **RO-1**, **2**, and **3** as photocatalysts (Figure S27). To explore the reasons for the different photocatalytic properties of **RO-1**, **2**, and **3**, the charge separation efficiencies of **RO-1**, **2**, and **3** were measured by transient photocurrent response under periodic light irradiation. As we can see in Figure S28, the photocurrent profiles showed **RO-1** had unattenuated and more sharp current than **RO-2** or **RO-3**, which reflected the higher separating and transfer efficiency of photoinduced electron−hole pairs in **RO-1**. The successively increasing resistance values of **RO-1**, **2**, and **3** obtained from EIS Nyquist plots also indicated that the photogenerated electrons are easier to migrate in **RO-1** (Figure S29). Besides, the lowest PL intensity of **RO-1** revealed its better suppressed radiative electron−hole recombination than **RO-2** and **RO-3**, which is consistent with the previous reports[47,48] (Figure S30). The effects of different qualities of **RO-1** on the photocatalytic CO_2 reduction performance in 10 h were further examined (Figure 3b). The highest CO evolution for 2 mg catalysts was 15.5 μmol/g/h (correspond to reduction yield: 7.6 μL). When the quality of catalysts was added to 5 mg, the catalytic rate of CO was slightly reduced to 13.8 μmol/g/h (16.9 μL). When the catalysts continued increased to 10 and 20 mg, the catalytic rate decreased significantly to 8 and 4.1 μmol/g·h, respectively, which were mainly affected by the contact area of CO_2 with a solid catalyst.

In this regard, we use 5 mg **RO-1** to evaluate the cyclic performance. In the cycle tests, we only refilled the saturated CO_2 and replaced fresh water for another 10-h light irradiation. **RO-1**, **2**, and **3** retain at least 90% of their original activity after four cycles (Figure 3c, S31, and S32). The photocatalytic durability was further evaluated by the long-time test. After 30 h of continuous exposure, the yields of CO were 398.7 (**RO-1**), 345.0 (**RO-2**), and 143.1 μmol/g (**RO-3**), manifesting that these **RO** cluster-based compounds have outstanding photocatalytic stability (Figure S33). What's more, the PXRD patterns (Figure S34), Fourier transform infrared spectroscopy (FTIR) curves (Figures S35−S37), and XPS spectra (Figure S38) before and after cyclic experiments were not apparently changed, which proved the structural stability of **RO-1**, **2**, and **3** during the photocatalytic process.

In order to prove the **RO** cluster-based photocatalysts did work during the artificial photosynthesis, a series of comparative experiments were carried out, and the results are presented in Figure 3d and Table S3. No product was detected when the system was placed in the dark, revealing that the reaction was a light-driven process. When the system was in the absence of H_2O, only traces of CO were observed by GC, which can be explained by the participation of original water molecules in the skeletons. Besides, compared with $\{PMo_8V_6O_{42}\}$[49] (Figure S39) (5.5 μmol/g/h) or $H_3PMo_{12}O_{40}{\cdot}xH_2O$ (4.3 μmol/g/h), the structure coupling with reduction clusters had the higher performance of photocatalytic reaction. This suggests that efficient electron−hole separation may happen in RO photocatalysts under light irradiation to achieve a longer lifetime. The physical mixture of MoO_3, V_2O_5, and MCl_2 ($ZnCl_2$/$CoCl_2$/$NiCl_2$) was also examined, and the CO evolution was less than **RO-1**, **2**, and **3**, revealing the superiority of the coordination network. Beyond that, compared with the condition of a pure CO_2 atmosphere, experiments under low concentration CO_2 (30% CO_2 + 70% Ar) were also performed (Figure 3e) which has more practical significance. It can be found that the photocatalysts still had good activity under an atmosphere of 30% CO_2 due to the adsorption capacity of CO_2 on the catalyst surface.

To further confirm that the CO and O_2 products were indeed converted from CO_2 and H_2O, $^{13}CO_2$ and $H_2{}^{18}O$ were used for isotopic tracing experiments to search for the source of C in CO and O in O_2 through gas chromatography mass spectrometry (GC-MS) analysis. Under the same test conditions, the signal at m/z 29 corresponding to ^{13}CO was detected, which demonstrated that the production of CO originated from CO_2 (Figure 3f). By comparing m/z of O_2 using $H_2{}^{16}O$ and $H_2{}^{18}O$ as a reagent, the apparent peak at 36 matching to $^{18}O_2$ suggested the produced O_2 was converted from $H_2{}^{18}O$ (Figures S40 and S41). Considering the above-mentioned points, it is proven that three **RO** cluster-based catalysts possess the ability to catalyze the artificial photosynthetic overall reaction.

Photoexcitation Process and Reaction Mechanism

To get insight into the photoexcitation process of **RO-1**, **2**, and **3** and further the intrinsic mechanism and the reaction pathways of artificial photosynthesis, the proposed catalytic processes were studied by TDDFT (cluster calculations) and free energy profiles (periodic calculations) (Figure S42). Figure 4a depicts

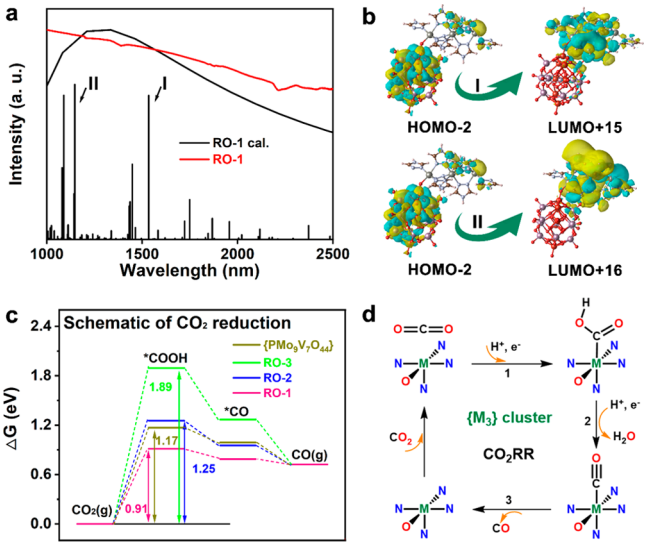

Figure 4. (a) Comparisons of experimental and calculated absorption spectra of **RO-1**. (b) Transitions from the $\{PMo_9V_7O_{44}\}$ fragment to the $\{\mathbf{M_3}\}$ part. (c) Free-energy profile for the CO_2RR pathway. (d) Proposed mechanism of CO_2RR catalyzed by **RO-1**, **2**, and **3** catalysts.

the simulated absorption spectrum and the measured solid UV−vis absorption of **RO-1**, showing a broad absorption in the near-infrared region due to a small band gap of the system (Figure S43). Based on the orbital transition analysis, the two strongest transitions in Figure 4a are mainly contributed by the transitions from the $\{PMo_9V_7O_{44}\}$ fragment to the $\{\mathbf{M_3}\}$ part (Figure 4b). Besides, internal transitions of $\{PMo_9V_7O_{44}\}$ and $\{\mathbf{M_3}\}$ can also be determined (Figures S44 and S45), which explains the weak

https://doi.org/10.1021/jacsau.1c00186
JACS Au 2021, 1, 1288−1295

photocatalytic performance of POM itself. The electron−hole separation from $\{PMo_9V_7O_{44}\}$ to $\{M_3\}$ endows **RO-1**, **2**, and **3** with higher catalytic activities. Next, to identify the reactive sites and deeply explore the difference of photoreaction properties among **RO-1**, **2**, and **3**, the Gibbs free energy (G) of the CO_2RR and WOR paths are compared. The conversion of the CO_2-to-CO reduction pathway contains three steps: CO_2 activation and hydrogenation (CO_2 → *COOH), dehydration (*COOH → *CO), and CO desorption (*CO → CO), where the first step has the highest positive energy difference acting as a rate-determining step (Figure 4c and Table S4). The energy change from CO_2 to *COOH on the Zn site (**RO-1**, 0.91 eV) is lower than Mo on the $\{PMo_8V_6O_{42}\}$ fragment, the Co site (**RO-2**, 1.25 eV), and Ni site (**RO-3**, 1.89 eV), implying the high activity of **RO-1** for CO_2 photoreduction. In addition, the higher free energy change for the formation of *H than *COOH on the Zn site of **RO-1** explains the high selectivity of CO production (Figure S46).

As for the process of water oxidation reaction, comparing the Gibbs free energy of each step, the first step of the adsorption of *OH intermediate is considered to be the potential-determinant step (Figure S47 and Table S4), and the computed ΔG values are as follows: $\Delta G_{RO\text{-}1}$ (1.51 eV) < $\Delta G_{RO\text{-}2}$ (1.71 eV) < $\Delta G_{RO\text{-}3}$ (1.89 eV). Hence, the H_2O-to-O_2 process can be achieved easily along with **RO-1** as photocatalyst. This is the reason why **RO-1** is one of the most suitable candidates for the artificial photosynthetic overall reaction. According to the above analysis, a credible photocatalytic mechanism is proposed (Figure 4d). When light illuminated on the catalysts, the polyoxometalate serving as the light harvester produces photogenerated electron−hole pairs. Then the photoelectrons transfer to the trinuclear cluster where the coordinately unsaturated metal ions act as reductive active site to convert CO_2 to CO. The photogenerated holes in the polyoxometalate are used to complete the water oxidation reaction.

■ CONCLUSION

In summary, we meticulously designed and synthesized three **RO** cluster-based catalysts (**RO-1**, **2**, and **3**), in which the independent and cooperative active clusters with reduction and oxidation can be used to complete the photocatalytic CO_2RR and WOR, respectively. Moreover, due to the more efficient electron transfer between the reduction and oxidation clusters along with their strong redox capabilities, **RO-1** exhibited the highest CO properties (138 μmol/g) in crystalline materials without any sacrificial agent, and the selectivity was close to 100%. Significantly, this work provides a feasible design strategy for constructing reduction−oxidation metal cluster-based compounds to be used as catalysts for artificial photosynthesis.

■ EXPERIMENTAL SECTION

Synthesis of RO-1 $[Zn_3(H_2O)_2(p\text{-}tr_2Ph)_5][PMo^V_5Mo^{VI}_4V^{IV}_7O_{44}]\cdot 8H_2O$

A mixture of p-tr_2Ph (15 mg, 0.07 mmol), NH_4VO_3 (15 mg, 0.13 mmol), $ZnCl_2$ (30 mg, 0.22 mmol), $Na_2MoO_4\cdot 2H_2O$ (50 mg, 0.21 mmol), H_3PO_3 (10 mg, 0.12 mmol), and H_2O (5 mL) was vigorous stirred for 30 min, transferred to a Teflon-lined stainless-steel reactor, and kept at 180 °C for 72 h. After 3 days, it was cooled down to 30 °C at a rate of 10 °C/h. The product was isolated by filtration, separated from an amorphous yellow powder and black block crystals of **RO-1** by decantation, then washed with distilled water; it was collected in 70% yield based on p-tr_2Ph. Anal. Calcd for $C_{50}H_{60}Zn_3Mo_9N_{30}O_{54}PV_7$ (Mw 3394.42): C, 17.68%; H, 1.77%; N, 12.37%. Found: C, 17.51%; H, 1.84%; N, 12.26%.

Synthesis of RO-2 $[Co_3(H_2O)_2(p\text{-}tr_2Ph)_5][PMo^V_5Mo^{VI}_4V^{IV}_7O_{44}]\cdot 10H_2O$

The preparation of **RO-2** was like the method of **RO-1**. Instead of $ZnCl_2$, $CoCl_2\cdot 6H_2O$ (30 mg, 0.12 mmol) as a substitute was added in solution. Finally, black rhombus crystals were obtained (40% yield based on p-tr_2Ph) and washed with distilled water. Anal. Calcd for $C_{50}H_{64}Co_3Mo_9N_{30}O_{56}PV_7$ (Mw 3411.13): C, 17.59%; H, 1.88%; N, 12.32%. Found: C, 17.33%; H, 1.94%; N, 12.16%.

Synthesis of RO-3 $[Ni_3(H_2O)_2(p\text{-}tr_2Ph)_5][PMo^V_5Mo^{VI}_4V^{IV}_7O_{44}]\cdot 6.5H_2O$

The preparation of **RO-3** was similar to the method used for **RO-1**. Instead of $ZnCl_2$, $NiCl_2\cdot 6H_2O$ (30 mg, 0.12 mmol) as a substitute was added in solution. Finally, black rhombus crystals were obtained (60% yield based on p-tr_2Ph) and washed with distilled water. Anal. Calcd for $C_{50}H_{57}Ni_3Mo_9N_{30}O_{52.5}PV_7$ (*Mw*: 3341.36): C, 17.96%; H, 1.71%; N, 12.57%. Found: C, 17.75%; H, 1.86%; N, 12.44%.

Synthesis of $\{PMo_8V_6O_{42}\}$ $[H_2N(C_2H_4)_2NH_2]_4(H_3O)[PMo^V_2Mo^{VI}_6V^{IV}_4O_{40}(V^{IV}O)_2]\cdot xH_2O$

$\{PMo_8V_6O_{42}\}$ is prepared based on previous reports with slight modifications. A mixture of NH_4VO_3 (73 mg, 0.625 mmol), $Na_2MoO_4\cdot 2H_2O$ (151 mg, 0.625 mmol), H_3PO_4 (72 μL, 1.25 mmol), $MnCl_2\cdot 4H_2O$ (123 mg, 0.625 mmol), piperazine (107.5 mg, 1.25 mmol), and H_2O (5 mL) was vigorously stirred for 30 min and transferred it to a Teflon-lined stainless-steel reactor and maintained at 150 °C for 144 h. After cooling to room temperature, black block crystals of $\{PMo_8V_6O_{42}\}$ were obtained (60% yield based on NH_4VO_3), washed with distilled water, and air-dried.

Photocatalytic Experiments

The crystals of **RO-1**, **2**, and **3** were washed with distill water and air-dried to be spared. Before photocatalytic reaction, the catalysts were ground into powder and weight 5 mg (or 2/10/20 mg). Then the powder was spread on a round-bottomed quartz crucible with ϕ20 mm and the quartz dish is placed in a 50 mL top-irradiation photocatalytic quartz reactor, which adds 0.2 mL distilled water as a sacrificial agent in the reactor. The reactor was ventilated for 20 min at a flow rate of 0.1 L/min under the test gas (pure CO_2, pure Ar, 30% CO_2 + 70% Ar) to ensure that the air in the reaction system was completely exchanged. During the overall reaction process, water will form a saturated vapor pressure in the system when exposed on a 300 W xenon lamp (λ = 300−1100 nm, light intensity 200 mW cm^{-2}); that is, the catalyst will only be in contact with water vapor and the test atmosphere. The experiments to evaluate the apparent quantum yield of CO of **RO-1**, **2**, and **3** were measured under monochromatic light (380 nm).

Isotopic Labeling Control Experiments

In isotope experiments, $^{13}CO_2$ was employed to confirm the carbon source of CO formed by photocatalytic CO_2 reduction and $H_2{}^{18}O$ was employed to confirm the oxygen source of product O_2. The ^{13}CO and $^{18}O_2$ were analyzed using gas chromatography mass spectrometry (GC-MS) (Figures 3f, S35, and S36).

Electrochemical Experiments

The electrochemical experiments (the Mott−Schottky plots and transient photocurrent response) are tested in a standard three-electrode system: indium−tin oxide conductive film glass (ITO glass, 1 cm × 2 cm) modified with catalyst samples, a carbon rod, and a Ag/AgCl electrode was employed as the working electrode, counter electrode, and the reference electrode, respectively. The Mott−Schottky plots were measured over an alternating current (AC) frequency of 1000, 1500, and 2000 Hz. The electrochemical impedance spectroscopy (EIS) plots were performed under similar conditions except using carbon cloth as the work electrode. The same bias voltage was set when EIS plots of **RO-1**, **2**, and **3** were performed. All of the electrochemical tests were performed in a 0.2 M Na_2SO_4 aqueous solution. PL spectra and were recorded by a FluoroMax-4 spectrofluorometer (Horiba Scientific).

https://doi.org/10.1021/jacsau.1c00186
JACS Au 2021, 1, 1288−1295

Sample Preparation of ITO Glass

The as-synthesized crystal (2 mg) was ground to a powder and then dispersed in 1 mL of solvent (990 μL ethanol and 10 μL 0.5% Nafion) by ultrasonication to form a homogeneous ink. Subsequently, 200 μL of the ink was dropped onto both sides of the ITO glass and dried at room temperature.

Density Functional Theory (DFT)

Periodic Calculations. The structure optimization and free energy calculations were performed within the framework of DFT as implemented in the Vienna Ab initio software package (VASP 5.3.5) code within the Perdew−Burke−Ernzerhof (PBE) generalized gradient approximation and the projected augmented wave (PAW) method.

Model Cluster Calculations. To perform time-dependent density-functional theory (TDDFT), a model cluster is constructed based on the optimized structure from periodic calculations. The cluster calculations are done by the ORCA package employing the resolution of identity approximation.

For detailed settings and results, please see the Supporting Information.

■ ASSOCIATED CONTENT

Supporting Information

The Supporting Information is available free of charge at https://pubs.acs.org/doi/10.1021/jacsau.1c00186.

Detailed information regarding the characterization analysis and electrochemical measurement (PDF)
Crystallographic information file for **RO-1** (CIF)
Crystallographic information file for **RO-2** (CIF)
Crystallographic information file for **RO-3** (CIF)

■ AUTHOR INFORMATION

Corresponding Authors

Jiang Liu − *Jiangsu Collaborative Innovation Centre of Biomedical Functional Materials, Jiangsu Key Laboratory of New Power Batteries, School of Chemistry and Materials Science, Nanjing Normal University, Nanjing 210023, P. R. China*; Email: liuj@njnu.edu.cn

Ya-Qian Lan − *School of Chemistry, South China Normal University, Guangzhou 510006, P. R. China; Jiangsu Collaborative Innovation Centre of Biomedical Functional Materials, Jiangsu Key Laboratory of New Power Batteries, School of Chemistry and Materials Science, Nanjing Normal University, Nanjing 210023, P. R. China;* orcid.org/0000-0002-2140-7980; Email: yqlan@m.scnu.edu.cn, yqlan@njnu.edu.cn; http://www.yqlangroup.com

Authors

Xiao-Xin Li − *School of Chemistry, South China Normal University, Guangzhou 510006, P. R. China; School of Chemistry and Chemical Engineering, Southeast University, Nanjing 211189, P. R. China*

Lei Zhang − *Jiangsu Collaborative Innovation Centre of Biomedical Functional Materials, Jiangsu Key Laboratory of New Power Batteries, School of Chemistry and Materials Science, Nanjing Normal University, Nanjing 210023, P. R. China*

Lin Yuan − *Jiangsu Collaborative Innovation Centre of Biomedical Functional Materials, Jiangsu Key Laboratory of New Power Batteries, School of Chemistry and Materials Science, Nanjing Normal University, Nanjing 210023, P. R. China*

Tong Wang − *Jiangsu Collaborative Innovation Centre of Biomedical Functional Materials, Jiangsu Key Laboratory of New Power Batteries, School of Chemistry and Materials Science, Nanjing Normal University, Nanjing 210023, P. R. China*

Jun-Yi Wang − *Jiangsu Collaborative Innovation Centre of Biomedical Functional Materials, Jiangsu Key Laboratory of New Power Batteries, School of Chemistry and Materials Science, Nanjing Normal University, Nanjing 210023, P. R. China*

Long-Zhang Dong − *Jiangsu Collaborative Innovation Centre of Biomedical Functional Materials, Jiangsu Key Laboratory of New Power Batteries, School of Chemistry and Materials Science, Nanjing Normal University, Nanjing 210023, P. R. China;* orcid.org/0000-0002-9276-5101

Kai Huang − *School of Chemistry and Chemical Engineering, Southeast University, Nanjing 211189, P. R. China;* orcid.org/0000-0002-5768-4189

Complete contact information is available at: https://pubs.acs.org/10.1021/jacsau.1c00186

Author Contributions

[⊥]X.-X.L. and L.Z. contributed equally to this work. Y.-Q.L., J.L., K.H., and X.-X.L. conceived and designed the idea. X.-X.L. synthesized the photocatalysts. L.Z. and X.-X.L. conducted the characterizations and designed the photocatalytic related experiments. L.Y., T.W., and J.-Y.W. assisted with the characterizations, designed the CO_2RR related experiments, collected the data. L.Z. and X.-X.L. analyzed the data. L.-Z.D. assisted with dealing with the data of SCXRD. Y.-Q.L., J.L., and X.-X.L. discussed the results and prepared the manuscript. All the authors reviewed and contributed to this paper.

Notes

The authors declare no competing financial interest.

■ ACKNOWLEDGMENTS

This work was financially supported by the NSFC (nos. 21622104, 92061101, 21871141, 21871142, and 21901122); the Natural Science Research of Jiangsu Higher Education Institutions of China (19KJB150011), and a project funded by China Postdoctoral Science Foundation (nos. 2018M630572 and 2019M651873); Priority Academic Program Development of Jiangsu Higher Education Institutions and the Foundation of Jiangsu Collaborative Innovation Center of Biomedical Functional Materials; The East-West Cooperation Project of Ningxia Key R & D Plan (no. 2019BFH02014); and Postgraduate Research & Practice Innovation Program of Jiangsu Province (KYCX20_1171).

■ REFERENCES

(1) Zhang, T.; Lin, W. Metal−organic frameworks for artificial photosynthesis and photocatalysis. *Chem. Soc. Rev.* **2014**, *43*, 5982−5993.

(2) Fang, X.; Kalathil, S.; Reisner, E. Semi-biological approaches to solar-to-chemical conversion. *Chem. Soc. Rev.* **2020**, *49*, 4926−4952.

(3) Yu, L.; Ba, X.; Qiu, M.; Li, Y.; Shuai, L.; Zhang, W.; Ren, Z.; Yu, Y. Visible-light driven CO_2 reduction coupled with water oxidation on Cl-doped Cu_2O nanorods. *Nano Energy* **2019**, *60*, 576−582.

(4) Zhang, M.; Lu, M.; Lang, Z.-L.; Liu, J.; Liu, M.; Chang, J.-N.; Li, L.-Y.; Shang, L.-J.; Wang, M.; Li, S.-L.; Lan, Y.-Q. Semiconductor/Covalent-Organic-Framework Z-Scheme Heterojunctions for Artificial Photosynthesis. *Angew. Chem., Int. Ed.* **2020**, *59*, 6500−6506.

(5) Kim, W.; McClure, B. A.; Edri, E.; Frei, H. Coupling carbon dioxide reduction with water oxidation in nanoscale photocatalytic assemblies. *Chem. Soc. Rev.* **2016**, *45*, 3221−3243.

(6) Hunter, B. M.; Gray, H. B.; Müller, A. M. Earth-Abundant Heterogeneous Water Oxidation Catalysts. *Chem. Rev.* **2016**, *116*, 14120−14136.
(7) Zhao, G.; Huang, X.; Wang, X.; Wang, X. Progress in catalyst exploration for heterogeneous CO_2 reduction and utilization: a critical review. *J. Mater. Chem. A* **2017**, *5*, 21625−21649.
(8) Sakimoto, K. K.; Wong, A. B.; Yang, P. Self-photosensitization of nonphotosynthetic bacteria for solar-to-chemical production. *Science* **2016**, *351*, 74−77.
(9) Woolerton, T.; Sheard, S.; Pierce, E.; Ragsdale, S.; Armstrong, F. CO_2 photoreduction at enzyme-modified metal oxide nanoparticles. *Energy Environ. Sci.* **2011**, *4*, 2393−2399.
(10) Wang, Y.; Zhang, Z.; Zhang, L.; Luo, Z.; Shen, J.; Lin, H.; Long, J.; Wu, J. C. S.; Fu, X.; Wang, X.; Li, C. Visible-Light Driven Overall Conversion of CO_2 and H_2O to CH_4 and O_2 on 3D-SiC@2D-MoS_2 Heterostructure. *J. Am. Chem. Soc.* **2018**, *140*, 14595−14598.
(11) Sasan, K.; Lin, Q.; Mao, C.; Feng, P. Open framework metal chalcogenides as efficient photocatalysts for reduction of CO_2 into renewable hydrocarbon fuel. *Nanoscale* **2016**, *8*, 10913−10916.
(12) Xiong, X.; Mao, C.; Yang, Z.; Zhang, Q.; Waterhouse, G. I. N.; Gu, L.; Zhang, T. Photocatalytic CO_2 Reduction to CO over Ni Single Atoms Supported on Defect-Rich Zirconia. *Adv. Energy Mater.* **2020**, *10*, 2002928.
(13) Liang, L.; Li, X.; Sun, Y.; Tan, Y.; Jiao, X.; Ju, H.; Qi, Z.; Zhu, J.; Xie, Y. Infrared Light-Driven CO_2 Overall Splitting at Room Temperature. *Joule* **2018**, *2*, 1004−1016.
(14) Jiang, H.; Katsumata, K.-i.; Hong, J.; Yamaguchi, A.; Nakata, K.; Terashima, C.; Matsushita, N.; Miyauchi, M.; Fujishima, A. Photocatalytic reduction of CO_2 on Cu_2O-loaded Zn-Cr layered double hydroxides. *Appl. Catal., B* **2018**, *224*, 783−790.
(15) Yu, F.; Wang, C.; Li, Y.; Ma, H.; Wang, R.; Liu, Y.; Suzuki, N.; Terashima, C.; Ohtani, B.; Ochiai, T.; Fujishima, A.; Zhang, X. Photothermal Catalysis: Enhanced Solar Photothermal Catalysis over Solution Plasma Activated TiO_2. *Adv. Sci.* **2020**, *7*, 2070092.
(16) Qian, Y.; Li, D.; Han, Y.; Jiang, H.-L. Photocatalytic Molecular Oxygen Activation by Regulating Excitonic Effects in Covalent Organic Frameworks. *J. Am. Chem. Soc.* **2020**, *142*, 20763−20771.
(17) Zhong, W.; Sa, R.; Li, L.; He, Y.; Li, L.; Bi, J.; Zhuang, Z.; Yu, Y.; Zou, Z. A Covalent Organic Framework Bearing Single Ni Sites as a Synergistic Photocatalyst for Selective Photoreduction of CO_2 to CO. *J. Am. Chem. Soc.* **2019**, *141*, 7615−7621.
(18) Yang, S.; Hu, W.; Zhang, X.; He, P.; Pattengale, B.; Liu, C.; Cendejas, M.; Hermans, I.; Zhang, X.; Zhang, J.; Huang, J. 2D Covalent Organic Frameworks as Intrinsic Photocatalysts for Visible Light-Driven CO_2 Reduction. *J. Am. Chem. Soc.* **2018**, *140*, 14614−14618.
(19) Fang, Z.-B.; Liu, T.-T.; Liu, J.; Jin, S.; Wu, X.-P.; Gong, X.-Q.; Wang, K.; Yin, Q.; Liu, T.-F.; Cao, R.; Zhou, H.-C. Boosting Interfacial Charge-Transfer Kinetics for Efficient Overall CO_2 Photoreduction via Rational Design of Coordination Spheres on Metal−Organic Frameworks. *J. Am. Chem. Soc.* **2020**, *142*, 12515−12523.
(20) Jiang, Z.; Xu, X.; Ma, Y.; Cho, H. S.; Ding, D.; Wang, C.; Wu, J.; Oleynikov, P.; Jia, M.; Cheng, J.; Zhou, Y.; Terasaki, O.; Peng, T.; Zan, L.; Deng, H. Filling metal−organic framework mesopores with TiO_2 for CO_2 photoreduction. *Nature* **2020**, *586*, 549−554.
(21) Rao, H.; Schmidt, L. C.; Bonin, J.; Robert, M. Visible-light-driven methane formation from CO_2 with a molecular iron catalyst. *Nature* **2017**, *548*, 74−77.
(22) Huang, Y.-B.; Liang, J.; Wang, X.-S.; Cao, R. Multifunctional metal−organic framework catalysts: synergistic catalysis and tandem reactions. *Chem. Soc. Rev.* **2017**, *46*, 126−157.
(23) Zhang, W.-X.; Liao, P.-Q.; Lin, R.-B.; Wei, Y.-S.; Zeng, M.-H.; Chen, X.-M. Metal cluster-based functional porous coordination polymers. *Coord. Chem. Rev.* **2015**, *293−294*, 263−278.
(24) Zeng, L.; Wang, Z.; Wang, Y.; Wang, J.; Guo, Y.; Hu, H.; He, X.; Wang, C.; Lin, W. Photoactivation of Cu Centers in Metal−Organic Frameworks for Selective CO_2 Conversion to Ethanol. *J. Am. Chem. Soc.* **2020**, *142*, 75−79.
(25) Dong, L.-Z.; Zhang, L.; Liu, J.; Huang, Q.; Lu, M.; Ji, W.-X.; Lan, Y.-Q. Stable Heterometallic Cluster-Based Organic Framework Catalysts for Artificial Photosynthesis. *Angew. Chem., Int. Ed.* **2020**, *59*, 2659−2663.
(26) Li, N.; Liu, J.; Liu, J.-J.; Dong, L.-Z.; Li, S.-L.; Dong, B.-X.; Kan, Y.-H.; Lan, Y.-Q. Self-Assembly of a Phosphate-Centered Polyoxo-Titanium Cluster: Discovery of the Heteroatom Keggin Family. *Angew. Chem., Int. Ed.* **2019**, *58*, 17260−17264.
(27) Benseghir, Y.; Lemarchand, A.; Duguet, M.; Mialane, P.; Gomez-Mingot, M.; Roch-Marchal, C.; Pino, T.; Ha-Thi, M.-H.; Haouas, M.; Fontecave, M.; Dolbecq, A.; Sassoye, C.; Mellot-Draznieks, C. Co-immobilization of a Rh Catalyst and a Keggin Polyoxometalate in the UiO-67 Zr-Based Metal−Organic Framework: In Depth Structural Characterization and Photocatalytic Properties for CO2 Reduction. *J. Am. Chem. Soc.* **2020**, *142*, 9428−9438.
(28) Saito, D.; Yamazaki, Y.; Tamaki, Y.; Ishitani, O. Photocatalysis of a Dinuclear Ru(II)−Re(I) Complex for CO_2 Reduction on a Solid Surface. *J. Am. Chem. Soc.* **2020**, *142*, 19249−19258.
(29) Zhang, H.-X.; Hong, Q.-L.; Li, J.; Wang, F.; Huang, X.; Chen, S.; Tu, W.; Yu, D.; Xu, R.; Zhou, T.; Zhang, J. Isolated Square-Planar Copper Center in Boron Imidazolate Nanocages for Photocatalytic Reduction of CO_2 to CO. *Angew. Chem., Int. Ed.* **2019**, *58*, 11752−11756.
(30) Li, N.; Liu, J.-J.; Sun, J.-W.; Dong, B.-X.; Dong, L.-Z.; Yao, S.-J.; Xin, Z.; Li, S.-L.; Lan, Y.-Q. Calix[8]arene-constructed stable polyoxo-titanium clusters for efficient CO2 photoreduction. *Green Chem.* **2020**, *22*, 5325−5332.
(31) Martin-Sabi, M.; Soriano-López, J.; Winter, R. S.; Chen, J.-J.; Vilà-Nadal, L.; Long, D.-L.; Galán-Mascarós, J. R.; Cronin, L. Redox tuning the Weakley-type polyoxometalate archetype for the oxygen evolution reaction. *Nat. Catal.* **2018**, *1*, 208−213.
(32) Lv, H.; Geletii, Y. V.; Zhao, C.; Vickers, J. W.; Zhu, G.; Luo, Z.; Song, J.; Lian, T.; Musaev, D. G.; Hill, C. L. Polyoxometalate water oxidation catalysts and the production of green fuel. *Chem. Soc. Rev.* **2012**, *41*, 7572−7589.
(33) Wang, S.-S.; Yang, G.-Y. Recent Advances in Polyoxometalate-Catalyzed Reactions. *Chem. Rev.* **2015**, *115*, 4893−4962.
(34) Zhang, Y.; Liu, J.; Li, S.-L.; Su, Z.-M.; Lan, Y.-Q. Polyoxometalate-based materials for sustainable and clean energy conversion and storage. *EnergyChem.* **2019**, *1*, 100021.
(35) Jin, L.; Li, X. X.; Qi, Y. J.; Niu, P. P.; Zheng, S. T. Giant Hollow Heterometallic Polyoxoniobates with Sodalite-Type Lanthanide-Tungsten-Oxide Cages: Discrete Nanoclusters and Extended Frameworks. *Angew. Chem., Int. Ed.* **2016**, *55*, 13793−13797.
(36) Xie, S. L.; Liu, J.; Dong, L. Z.; Li, S. L.; Lan, Y. Q.; Su, Z. M. Hetero-metallic active sites coupled with strongly reductive polyoxometalate for selective photocatalytic CO_2-to-CH_4 conversion in water. *Chem. Sci.* **2019**, *10*, 185−190.
(37) Chen, W.-B.; Leng, J.-D.; Wang, Z.-Z.; Chen, Y.-C.; Miao, Y.; Tong, M.-L.; Dong, W. Reversible crystal-to-crystal transformation from a trinuclear cluster to a 1D chain and the corresponding spin crossover (SCO) behaviour change. *Chem. Commun.* **2017**, *53*, 7820−7823.
(38) Ding, B.; Yang, E.-C.; Zhao, X.-J.; Wang, X. G. A linear trinuclear cobalt(II) complex with 4-(2-pyridine)-1,2,4-triazole: synthesis, structure and characterization. *J. Coord. Chem.* **2008**, *61*, 3793−3799.
(39) Gómez, V.; Sáenz de Pipaón, C.; Maldonado-Illescas, P.; Waerenborgh, J. C.; Martin, E.; Benet-Buchholz, J.; Galán-Mascarós, J. R. Easy Excited-State Trapping and Record High TTIESST in a Spin-Crossover Polyanionic FeII Trimer. *J. Am. Chem. Soc.* **2015**, *137*, 11924−11927.
(40) Li, X.-M.; Dong, L.-Z.; Liu, J.; Ji, W.-X.; Li, S.-L.; Lan, Y.-Q. Intermediate-Temperature Anhydrous High Proton Conductivity Triggered by Dynamic Molecular Migration in Trinuclear Cluster Lattice. *Chem.* **2020**, *6*, 2272−2282.
(41) Yang, C.; Zhu, Q.; Sadakane, M.; Zhang, Z.; Li, Y.; Ueda, W. Vanadium-Enhanced Intramolecular Redox Property of a Transition-Metal Oxide Molecular Wire. *Inorg. Chem.* **2020**, *59*, 16557−16566.
(42) Weinstock, I. A.; Schreiber, R. E.; Neumann, R. Dioxygen in Polyoxometalate Mediated Reactions. *Chem. Rev.* **2018**, *118*, 2680−2717.

https://doi.org/10.1021/jacsau.1c00186
JACS Au 2021, 1, 1288−1295

(43) Liu, J.; Liu, Y.; Liu, N.; Han, Y.; Zhang, X.; Huang, H.; Lifshitz, Y.; Lee, S.-T.; Zhong, J.; Kang, Z. Metal-free efficient photocatalyst for stable visible water splitting via a two-electron pathway. *Science* **2015**, *347*, 970−974.
(44) Hou, W.; Hung, W. H.; Pavaskar, P.; Goeppert, A.; Aykol, M.; Cronin, S. B. Photocatalytic Conversion of CO_2 to Hydrocarbon Fuels via Plasmon-Enhanced Absorption and Metallic Interband Transitions. *ACS Catal.* **2011**, *1*, 929−936.
(45) Xiang, Q.; Cheng, B.; Yu, J. Graphene-Based Photocatalysts for Solar-Fuel Generation. *Angew. Chem., Int. Ed.* **2015**, *54*, 11350−11366.
(46) Li, R.; Zhang, W.; Zhou, K. Metal−Organic-Framework-Based Catalysts for Photoreduction of CO2. *Adv. Mater.* **2018**, *30*, 1705512.
(47) Men, Y.-L.; You, Y.; Pan, Y.-X.; Gao, H.; Xia, Y.; Cheng, D.-G.; Song, J.; Cui, D.-X.; Wu, N.; Li, Y.; Xin, S.; Goodenough, J. B. Selective CO Evolution from Photoreduction of CO_2 on a Metal-Carbide-Based Composite Catalyst. *J. Am. Chem. Soc.* **2018**, *140*, 13071−13077.
(48) Xu, H.-Q.; Hu, J.; Wang, D.; Li, Z.; Zhang, Q.; Luo, Y.; Yu, S.-H.; Jiang, H.-L. Visible-Light Photoreduction of CO_2 in a Metal−Organic Framework: Boosting Electron−Hole Separation via Electron Trap States. *J. Am. Chem. Soc.* **2015**, *137*, 13440−13443.
(49) Li, Y.; Wang, E.; Wang, S.; Duan, Y.; Hu, C.; Hu, N.; Jia, H. A highly reduced polyoxoanion with phosphorus-centered alternate layers of Mo/V oxides, $[PMo_2{}^{V}Mo_6{}^{VI}V_4{}^{IV}O_{40}(V^{IV}O)_2]^{9-}$. *J. Mol. Struct.* **2002**, *611*, 185−191.

https://doi.org/10.1021/jacsau.1c00186
JACS Au 2021, 1, 1288−1295